Applied Thermal Engineering 280 (2025) 128353

Contents lists available at ScienceDirect

Applied Thermal Engineering

journal homepage: www.elsevier.com/locate/apthermeng

Research Paper

Boiling dynamics in microporous copper-coated manifold microchannels

Youngseob Lee [a,1], Daeyoung Kong [b,1], Jaewon Hwang [c], Seokwon Jeong [a], Jungwan Cho [d], Hyoungsoon Lee [a,c,*]

[a] Department of Intelligent Energy and Industry, Chung-Ang University, Seoul 06974, South Korea
[b] Department of Mechanical Engineering, Stanford University, Stanford, CA 94305, USA
[c] School of Mechanical Engineering, Chung-Ang University, Seoul 06974, South Korea
[d] School of Mechanical Engineering, Sungkyunkwan University, Suwon-si, Gyeonggi-do 16419, South Korea

ARTICLE INFO

Keywords:
Boiling dynamics
Manifold microchannel
Copper inverse opal
Two-phase convection
Bubble behavior
Critical heat flux

ABSTRACT

The rapid densification of AI semiconductors and the proliferation of data centers have significantly increased the demand for advanced thermal management solutions. Employing manifold microchannels (MMCs) in two-phase embedded cooling systems has emerged as an effective method to address these thermal challenges. However, a comprehensive understanding of the flow characteristics within these systems remains limited, especially for performance optimization and triggers of critical heat flux (CHF) due to the complex liquid–vapor interactions occurring in three-dimensional cooling structures. This study investigates the flow boiling behavior in MMCs coated with copper inverse opals (CuIOs), utilizing Novec-649 as the working fluid. Experiments are performed at mass fluxes of 1000 and 2000 kg m^{-2} s^{-1} within microchannels having aspect ratios of 0.5, 1, and 2. The CuIO coatings enhance nucleate boiling and stabilize liquid film dynamics by providing interconnected porous structures, thus effectively delaying dry-out phenomena, achieving a maximum CHF of 237 W cm^{-2}. Furthermore, the study elucidates flow dynamics linked to heat transfer coefficients, thermal resistance, and mechanisms underlying flow-induced instabilities, emphasizing bubble behavior and its critical role in CHF initiation. In-situ visualization provides direct observations of CHF-triggering mechanisms, including bubble confinement and backflow induced by flow non-uniformity, highlighting that the instability characteristics vary significantly depending on microchannel geometry. These findings contribute critical insights into the two-phase flow phenomena within MMC systems, offering practical guidelines for tailoring channel geometry and surface coatings to enhance thermal management capability in embedded cooling solutions for high heat flux electronic applications.

1. Introduction

Recent advances in AI chiplet technologies and the rapid expansion of data centers have significantly increased integration densities and driven heterogeneous integration, leading to substantial thermal management challenges [1,2]. These technological trends introduce multiple heat sources and larger chip sizes, posing challenges in effectively dissipating high heat loads across extensive areas while minimizing cooling energy consumption [3]. Thermal management complexities are further exacerbated by thermal crosstalk between high-bandwidth memory and logic components, demanding precise temperature uniformity to ensure system reliability and electrical efficiency [4,5]. Consequently, advanced cooling strategies capable of addressing these rigorous demands have become increasingly vital.

Two-phase heat transfer has gained substantial interest due to its superior heat dissipation capability, leveraging the latent heat of vaporization to significantly improve cooling performance [6]. However, traditional two-phase cooling methods, such as straight microchannels, micro-pin fins, multi-jet impingement, and spray cooling, face critical limitations, including pronounced temperature non-uniformities, excessive pressure drops, and inherent flow instabilities under two-phase conditions [7–11]. Thus, innovative approaches offering both enhanced thermal management performance and operational stability are urgently required.

Manifold microchannel (MMC) heat sinks have emerged as promising solutions, efficiently managing heat removal while significantly reducing pumping power and maintaining relatively low pressure drops

* Corresponding author at: Department of Intelligent Energy and Industry, Chung-Ang University, Seoul 06974, South Korea.
E-mail address: leeh@cau.ac.kr (H. Lee).

[1] The authors who are equally contributed to this work.

https://doi.org/10.1016/j.applthermaleng.2025.128353
Received 30 June 2025; Received in revised form 27 August 2025; Accepted 13 September 2025
Available online 15 September 2025
1359-4311/

Nomenclature

A	area (m^2)
c_p	specific heat ($J\ kg^{-1}\ K^{-1}$)
D_h	hydraulic diameter (m)
G	mass flux ($kg\ m^{-2}\ s^{-1}$)
H	height (m)
h	heat transfer coefficient ($W\ m^{-2}\ K^{-1}$)
h_{lv}	latent heat ($kJ\ kg^{-1}$)
I	electrical current (A)
k	thermal conductivity ($W\ m^{-1}\ K^{-1}$)
$\dot{m}$	mass flow rate ($g\ min^{-1}$)
N	number of channels
ΔP	pressure drop (kPa)
q“	heat flux ($W\ cm^{-2}$)
q^*	ratio of heat flux to critical heat flux
R	thermal resistance ($cm^2\ K\ W^{-1}$)
T	temperature (K)
T	thickness (m)
V	electrical voltage (V)
W	width (m)
x	outlet thermodynamic equilibrium quality
Greek Letter	
ε	emissivity
η	fin efficiency
ρ	density ($kg\ m^{-3}$)
σ	surface tension ($mN\ m^{-1}$)
Subscripts	
adv	advection
avg	average
b	base
ch	channel
cond	conduction
conv	convection
f	fluid
h	heater
in	inlet
l	liquid
loss	heat loss
m	manifold
o	overall
out	outlet
sat	saturated
si	silicon
tot	total
v	vapor
w	wall
wet	wetted

[12,13]. MMCs circumvent the inherent shortcomings of conventional microchannel designs by shortening fluid flow paths and strategically utilizing jet impingement on heated surfaces to boost convective heat transfer. Comprehensive full-scale studies have validated the effectiveness of MMC designs under realistic thermal–hydraulic conditions, demonstrating significantly reduced thermal resistance values and improved operational stability even at high heat flux levels [14,15]. Notably, infrared visualization experiments have demonstrated increasing thermal gradients among multi-chip arrangements under elevated heat fluxes in two-phase flow regimes, highlighting persistent thermal management challenges within MMCs [14]. Additionally, studies reported that local dry-out phenomena restrict heat transfer efficiency at elevated heat flux conditions, despite initial improvements with increasing flux levels [15]. Moreover, the relationship between flow rate and thermal resistance in MMC systems exhibits a non-monotonic behavior, reflecting a transition from traditional channel convection to enhanced jet impingement as the flow velocity increases. This reveals the intricate thermal-fluid dynamics within these systems [16]. Although structural enhancements including staggered pin fins and nanowires have shown beneficial effects, internal visualization of two-phase flows in complex MMC geometries remains limited, hindering deeper understanding of flow instabilities and heat transfer mechanisms. Nonetheless, these studies remained limited due to an inability to visualize internal two-phase flow dynamics within complex MMC geometries, constraining deeper insight into instability and flow mechanisms.

To overcome such constraints, recent research employed simplified, custom-fabricated MMC unit cells integrated with manifolds, enabling detailed visualization and fundamental exploration of two-phase flow phenomena. Detailed visualization studies have provided critical insights into local temperature distributions by identifying boiling suppression mechanisms caused by jet impingement and vapor blanket formation effects hindering liquid rewetting in deeper channel configurations [17]. Additionally, topology-optimized MMC unit cells have demonstrated their ability to stabilize bubbly and confined flow regimes, effectively delaying undesirable slug flow transitions despite slightly reduced two-phase heat transfer coefficients [18].

Despite these advancements, existing studies have not yet explained the detailed two-phase flow dynamics that govern the coupled performance of critical heat flux (CHF) and heat transfer coefficient, nor the mechanisms underlying CHF initiation in practical MMC devices. Although the trade-off between CHF and heat transfer coefficient during boiling is well recognized, a comprehensive physical interpretation is still missing, especially in relation to the role of liquid film dynamics. Moreover, previous explanations that do not account for the temporal and spatial conditions of CHF fail to capture the complexity inherent in MMC structures. Clarifying these interactions is essential for both advancing fundamental understanding and guiding the practical design of MMC cooling technologies. To address this critical gap, the present study systematically investigates flow boiling characteristics in MMCs enhanced with microporous copper inverse opals (CuIO), which are known to significantly promote nucleation activity and stabilize liquid films [19,20]. Using in-situ visualization techniques, this work elucidates how microchannel geometry and surface modifications affect liquid film behavior, bubble dynamics, flow instabilities, and ultimately CHF triggering mechanisms, thereby providing important insights for optimizing thermal management in high heat flux electronic applications.

2. Experimental method

2.1. CuIO-coated microchannel fabrication

The fabrication process for the CuIO-coated microchannels involves two main stages: (1) fabrication of the silicon microchannels integrated with heaters and electrodes, and (2) formation of porous CuIO structures via template-assisted electrodeposition.

Initially, three different microchannel geometries were fabricated on a 6-inch silicon wafer using deep reactive ion etching (Fig. 1a). Each microchannel configuration shared an identical footprint (5 × 5 mm^2) but differed in channel widths (50, 100, and 200 μm, Fig. S1). A serpentine heater composed of Ti/Au layers (20 nm/200 nm) was deposited on the backside of the silicon wafer, forming an integrated heating platform. An additional Ti/Au electrode layer was sputtered

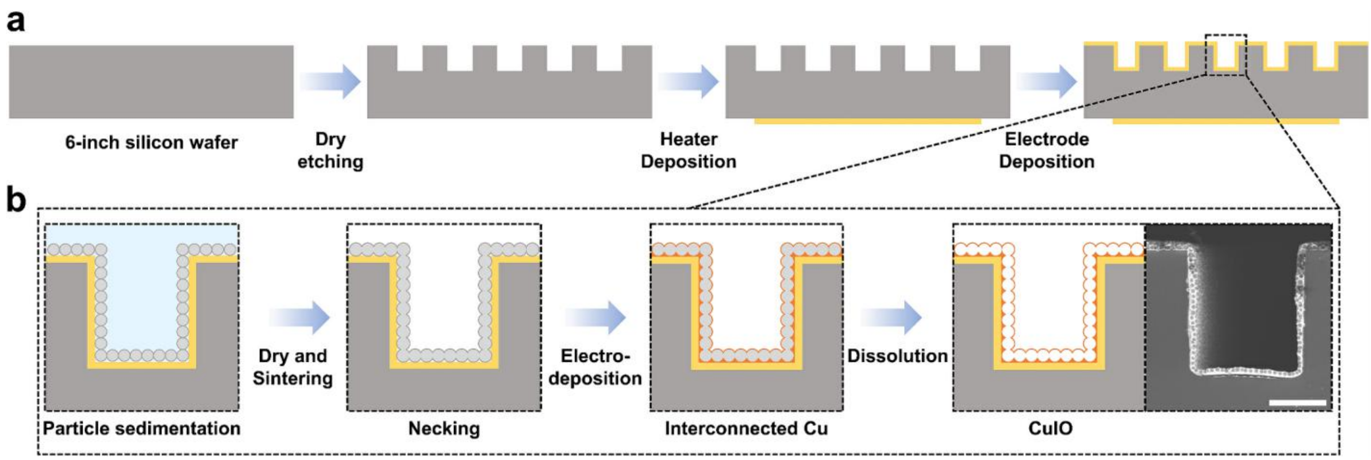

Fig. 1. Schematic illustration of the fabrication process for CuIO-coated manifold microchannels: **a,** Microchannel fabrication steps including DRIE etching, backside heater deposition, and electrode layer formation, and **b,** Templated electrodeposition process for porous CuIOs, showing polystyrene particle self-assembly by sedimentation, sintering, copper electrodeposition, and template removal. A scale bar is 50 μm.

onto the microchannel surfaces to enable copper electrodeposition.

Microporous CuIO coatings were fabricated onto the microchannel surfaces through template-assisted electrodeposition (Fig. 1b). Polystyrene spheres (5.0 μm diameter, 5.0 % w v^{-1}) were dispersed onto gold-coated microchannel substrates and dried at 60 °C, forming densely packed structures. Sintering at 100 °C for 80 min produced interconnected porous templates with controlled pore sizes (~5.0 μm) and neck diameters (~1.5 μm) (Fig. S2), conditions previously optimized for efficient boiling with an estimated porosity of ~0.83 [21,22]. Importantly, SEM observations confirmed that these robust structures were preserved after the boiling experiments, showing no noticeable degradation in morphology (Fig. S3, Supplementary Notes S1). This result demonstrates that the CuIO coating maintained its structural integrity under the tested operating conditions. Copper was subsequently electrodeposited into these polystyrene templates at a current density of 2.5 mA cm^{-2} for 90 min, using a potentiostat (BioLogic, SP-300) with an oxygen-free copper block (anode), a gold-coated microchannel (cathode), and an electrolyte solution (0.5 M $CuSO_4$ + 0.2 M H_2SO_4 aqueous solution). A small amount of ethanol was added beforehand to improve electrolyte infiltration into the template. Finally, the polystyrene templates were completely removed by immersion in tetrahydrofuran for 24 h, yielding robust and interconnected porous copper structures designed to significantly enhance nucleate boiling performance.

2.2. Manifold microchannel test section

After completing the CuIO coating described in Section 2.1, the microchannels were integrated into the MMC test section (Fig. 2a). The test section consisted of CuIO-coated silicon microchannels, a polydimethylsiloxane (PDMS) manifold, a 3D-printed holder made of Rigid 10 K resin (Form 3, Formlabs Inc.), and a transparent polycarbonate (PC) housing block. The resin holder provided stable mechanical support, minimized thermal losses, and incorporated dedicated openings for electrical connections and temperature measurement.

The manifold structure was fabricated by molding PDMS using a micromachined PDMS mold and subsequently cured. Following oxygen plasma treatment, the PDMS manifold was securely bonded to the silicon microchannels to ensure leak-free fluid operation. The manifold had three inlet conduits and two outlet conduits arranged to enable perpendicular fluid flow onto the microchannel surfaces, thus enhancing convective heat transfer through jet impingement. The assembled structure was enclosed within a transparent PC housing block (thermal conductivity ~0.2 W m^{-1} K^{-1}), enabling direct visualization of two-phase boiling phenomena and providing integrated fluid inlet/outlet passages and measurement ports for temperature and pressure sensors. Detailed geometric information of the PDMS manifold and microchannels is provided in Fig. 2b, c and Table 1, while the overall flow paths are illustrated in Fig. 2d.

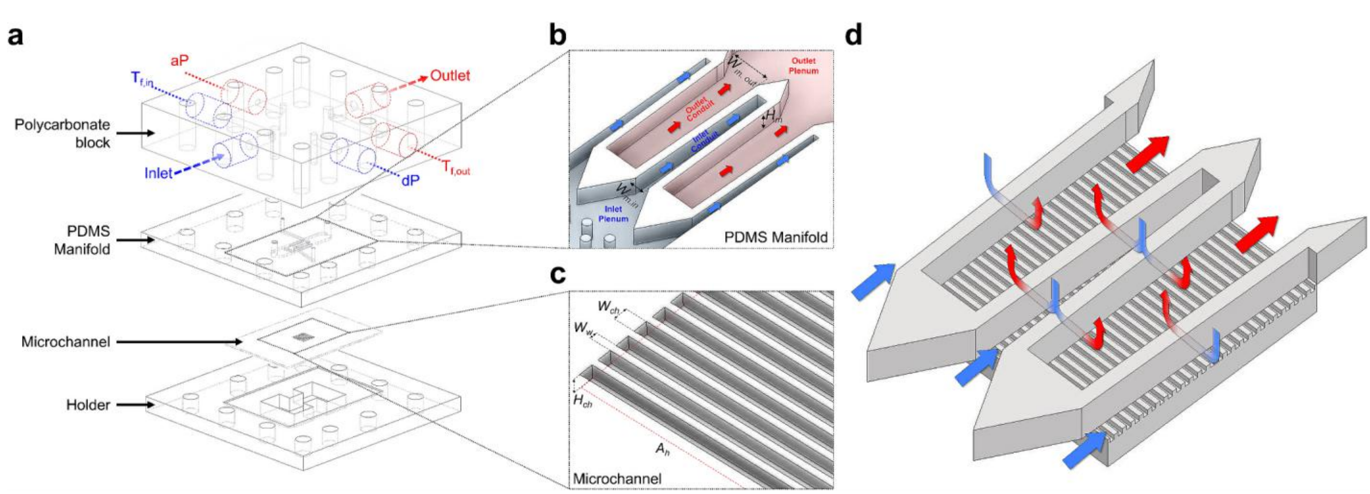

Fig. 2. Configuration of the test section. **a,** Exploded view of the test section showing PDMS manifold, CuIO-coated microchannels, holder, and PC housing, **b,** PDMS manifold with inlet/outlet plenums, **c,** Detailed geometry of silicon microchannels, and **d,** Total flow paths in the entire device.

Table 1
Geometrical conditions of the manifold and microchannels.

Parameters	Microchannels		
	MMC1	MMC2	MMC3
W_{ch}, [μm]	50	100	200
W_w, [μm]	100	100	100
H_{ch}, [μm]	100	100	100
N_{ch}	33	25	16
Aspect Ratio	2.0	1.0	0.5
–	Manifold		
$W_{m,in}$, [μm]	680		
$W_{m,out}$, [μm]	1380		
H_m, [μm]	900		

Table 2
Novec-649′s thermophysical properties at 1 atm.

Properties	Value
T_{sat}, [°C]	49.0
ρ_l, [kg m^{-3}]	1527.0
ρ_v, [kg m^{-3}]	12.8
c_p, [J kg^{-1} K^{-1}]	1122
k_f, [W m^{-1} K^{-1}]	0.054
h_{lv}, [kJ kg^{-1}]	88.0
σ, [mN m^{-1}]	8.4

2.3. Experimental setup

The assembled MMC test section described in Section 2.2 was integrated into a closed-loop circulation system (Fig. 3a). Prior to experiments, the dielectric working fluid (Novec-649; thermophysical properties in Table 2) was thoroughly degassed by simultaneous boiling and condensation processes within a reservoir. Immersion heaters and an internal condensing coil connected to a liquid-loop chiller (Jeiotech HH20) maintained stable thermal conditions and effectively removed dissolved gases. A magnetically driven gear pump (Micropump GA-T23) circulated the dielectric fluid, and mass flow rates were precisely measured using a Coriolis liquid flow meter (KIF-510). The fluid was preheated to achieve approximately 39.5 °C of subcooling at the test section inlet. After exiting the test section, the fluid was condensed and cooled via a heat exchanger connected to the chiller, ensuring stable inlet conditions.

Electrical power was supplied to silicon microchannels by a DC power supply (EX300-12), allowing precise control of voltage and current. Fluid temperatures at the manifold inlet and outlet were monitored with K-type thermocouples (OMEGA Eng., accuracy ± 1.1 °C), inserted into dedicated ports integrated into the PC housing. Heater surface temperature distributions were recorded by an infrared (IR) camera (FLIR A655sc, accuracy ± 2 °C), mounted beneath the test section. To ensure accuracy, the heater surface was coated with black paint, where its emissivity ($\varepsilon = 0.93$) was calibrated by attaching a thermocouple to the surface and comparing the thermocouple readings with those from the IR camera prior to testing. Differential (OMEGA PX409, accuracy ±0.25 %) and absolute (TRAFAG ECT8472, accuracy ±0.5 %) pressure transducers measured pressure drop and fluid saturation pressures, respectively. Flow boiling phenomena within microchannels were visualized from above using a high-speed camera (Photron FASTCAM Mini UX100, 4000 frames per second). An NI Compact data acquisition system collected voltage, current, and pressure data via the NI 9220 module, and temperature data via the NI 9214 module. All experimental parameters except base temperatures (IR camera data) were recorded using LabVIEW software. Actual images of the assembled experimental setup are shown in Fig. 3b and c.

Experiments were performed with the applied heat flux starting from 0 W cm^{-2} and increasing in about 10 W cm^{-2} increments. At each step, the system was allowed to reach a steady state before proceeding to the next level. This protocol continued until CHF was achieved, during which the heater temperatures were continuously monitored via IR measurements. Overall, the heat flux ranged from 0 to 240 W cm^{-2}, and the corresponding pressure drop varied from 5 to 35 kPa. Throughout the thermal fluid tests, mass flow rates of 38.4 to 153 g min^{-1}, which are equivalent to mass fluxes of 1000–2000 kg m^{-2} s^{-1} based on microchannel cross-sectional area. A fixed outlet pressure of 120–130 kPa and an inlet temperature of approximately 39.5 °C were held constant. Upon observing sudden temperature spikes, the power supply was immediately shut off while monitoring was carried out via real-time IR thermography and high-speed imaging. For more detailed information, the operation and result ranges of the hydraulic-thermal tests were summarized at Table 3.

2.4. Data reduction and uncertainties

Effective heat flux supplied to the microchannels was calculated by subtracting experimentally measured heat losses (<6.6 % of total input)

Table 3
Summary of geometries and thermal–hydraulic operating conditions.

Operating parameters	Ranges
Hydraulic diameter of microchannel, [μm]	$67 < D_{h,ch} < 133$
Subcooling temperature, [°C]	$39.3 < T_{f,in} < 39.7$
Mass flow rate, [g min^{-1}]	$38.4 < \dot{m} < 153.6$
Mass flux based on microchannels, [kg m^{-2} s^{-1}]	$1000 < G < 2000$
Heat flux, [W cm^{-2}]	$0 < q'' < 240$
Heat transfer coefficient, [W m^{-2} K^{-1}]	$11{,}000 < h < 32{,}500$
Pressure drop, [kPa]	$5 < \Delta P < 35$
Exit vapor quality	$0.02 < x < 0.43$

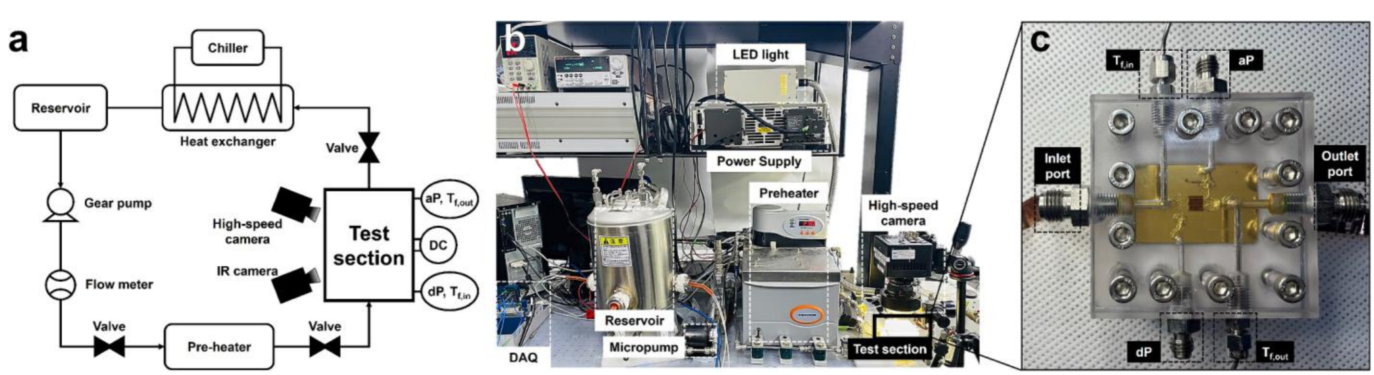

Fig. 3. Schematic overview of experimental setup: **a,** Schematic illustration of the closed-loop flow system, **b,** Photograph of the experimental apparatus, including DC power supply for Joule heating, data acquisition system, flow meter, and liquid-loop chiller, and **c,** Assembled test section showing transparent PC housing, PDMS manifold, and the connection of measurement sensors.

from total electrical power input. IR-measured heater surface temperatures were corrected for conduction losses through the silicon substrate, yielding accurate microchannel base temperatures. Superheat was calculated as the temperature difference between corrected base temperature and fluid saturation temperature from pressure measurements.

The two-phase heat transfer coefficient was computed by considering the overall fin efficiency, accounting for geometric parameters and convective conditions. Additionally, outlet thermodynamic vapor quality was determined using energy balances involving measured mass flow rates and fluid enthalpies. Thermophysical fluid properties (density, specific heat, thermal conductivity, latent heat, surface tension) were obtained from REFPROP 10.0 as temperature-dependent variables.

The total thermal resistance was decomposed into three individual components: conduction through the silicon substrate, convection at the microchannel surface, and advection by fluid flow. Pressure drops across the test section were directly measured using differential pressure sensors integrated into the housing block (Section 2.3). Detailed calculation procedures, equations, and thermophysical properties are provided in the Supplementary Notes S2.

Measurement uncertainties were calculated using standard error propagation methods based on instrument accuracies (summarized in Table 4). Voltage and current measurement uncertainties from the DC power supply (EX300-12) were ±450 mV and ±38 mA, respectively. The uncertainty in the heat transfer coefficient calculation was determined using uncertainties in the microchannel base temperature (T_b, ±2 °C via IR camera) and the average fluid temperature ($T_{f,avg}$, ±1.1 °C via thermocouples). Similarly, uncertainty in total thermal resistance (R_{tot}) was calculated based on uncertainties in the heater surface temperature (T_h, ±2 °C via IR camera) and fluid inlet temperature ($T_{f,in}$, ±1.1 °C via thermocouples). Pressure measurements had an uncertainty of ±0.25 %, based on the accuracy of the differential pressure sensor. Comprehensive details regarding the uncertainty calculation procedures are provided in the Supplementary Notes S3.

3. Results and discussion

3.1. Thermal performance characteristics

Fig. 4 presents boiling curves depicting heat flux as a function of superheat across varying mass fluxes and microchannel geometries. Initially, sensible heat transfer dominated, exhibiting a linear relationship between heat flux and superheat. Upon initiation of nucleate boiling, the sensitivity of heat flux to increasing superheat markedly decreased, predominantly influenced by enhanced nucleation from the CuIO coatings [23,24] and the advantageous thermophysical properties of Novec-649, including its low boiling temperature and reduced surface tension. [20,25]. Notably, a higher mass flux of 2000 kg m^{-2} s^{-1} delayed boiling initiation due to greater sensible heat capacity, requiring increased heat flux levels before two-phase heat transfer became dominant. Furthermore, CHF values improved consistently with increasing mass flux across all microchannel configurations. Among these, MMC2 achieved the highest CHF of approximately 237 W cm^{-2} at the 2000 kg m^{-2} s^{-1} condition, even though it experienced relatively elevated surface temperatures. Conversely, MMC1 and MMC3 exhibited comparable yet lower CHF values.

Table 4
Uncertainty propagation through experimental equipment and measurement.

Equipment	Parameters	Accuracy
DC power supply	V	±450 mV
	I	±38 mA
K-type thermocouple	$T_{f,in}$, $T_{f,out}$, $T_{f,avg}$	±1.1 °C
IR camera	T_b, T_h	±2 °C
Differential pressure transducer	ΔP	±0.25 %
Calculated parameters		Uncertainty
q"		<5.0 %
h		<10.9 %
R_{tot}		<8.5 %

Fig. 5 illustrates the base temperature distributions within MMC3 at two representative heat flux conditions of 42 and 134 W cm^{-2} under a mass flux of 2000 kg m^{-2} s^{-1}. The dimensionless parameter q^*, defined as the ratio of applied heat flux to CHF (q''/q''_{CHF}), corresponds to 0.20 and 0.65 at these heat fluxes, respectively, given a CHF value of 205 W cm^{-2} for MMC3. The heater surface temperatures obtained via IR thermography were corrected to account for conduction-related temperature drops through the silicon substrate. At the lower heat flux ($q^* = 0.20$), single-phase jet impingement cooling dominated near inlet regions, resulting in lower base temperatures compared to the outlet regions, where sensible heating was more pronounced [21]. In contrast, at the higher heat flux ($q^* = 0.65$), shown in Fig. 5b, this temperature distribution reversed, exhibiting elevated inlet temperatures due to significant pressure drops induced by vigorous bubble generation, causing local saturation temperature reductions along the fluid flow path [17].

Fig. 6a presents the heat transfer coefficients as functions of applied heat flux. At a mass flux of 1000 kg m^{-2} s^{-1}, the heat transfer coefficients increased notably with rising heat flux, achieving peak values near 28,000 W m^{-2} K^{-1} for MMC1, 21,000 W m^{-2} K^{-1} for MMC2, and 33,000 W m^{-2} K^{-1} for MMC3. Upon increasing the mass flux to 2000 kg m^{-2} s^{-1}, MMC1 and MMC3 displayed reductions in heat transfer coefficients, while MMC2 exhibited improved performance under the same heat flux conditions. At a representative heat flux of 100 W cm^{-2}, MMC1 and MMC3 showed decreases of roughly 14 % and 20 %, respectively, compared to their values at 1000 kg m^{-2} s^{-1}. In contrast, MMC2 demonstrated an increase of approximately 9 %, highlighting a dominant convective heat transfer mechanism linked to enhanced liquid velocities [26,27].

Fig. 6b illustrates the variation of heat transfer coefficients with exit vapor quality. Consistent with prior observations [14,15], heat transfer coefficients exhibited a concave trend as vapor quality increased, reflecting a shift from nucleate boiling to convection-dominated heat transfer accompanied by intermittent dry-out events. Consequently, the growth rate of heat transfer coefficients either diminished or sharply declined at elevated vapor qualities [28]. Increasing mass flux generally alleviated this decline; however, the extent of mitigation significantly differed among microchannels. MMC1 experienced the greatest decrease, approximately 18 % from the peak value near CHF conditions at 1000 kg m^{-2} s^{-1}, primarily due to limited liquid replenishment stemming from its higher aspect ratio, which limits effective liquid replenishment toward the channel base and promotes local dry-out [17]. Conversely, MMC3 consistently maintained high heat transfer coefficients around 33,000 W m^{-2} K^{-1} at both mass flux conditions, reflecting superior resistance to degradation due to its lower aspect ratio and enhanced liquid replenishment. MMC2 similarly showed reduced sensitivity to heat transfer deterioration due to balanced geometric conditions that favor stable convective flow.

Overall, MMC2 displayed lower heat transfer coefficients compared to MMC1 and MMC3, primarily arising from variations in liquid film thickness related to channel aspect ratios, as illustrated in Fig. 6c [29]. Within confined microchannel environments, liquid film thickness significantly depends on channel geometry, forming thinner films along elongated wall surfaces in rectangular channels [30,31]. Specifically, MMC1′s high aspect ratio promoted thinner liquid films along the narrow sidewalls, whereas MMC3, characterized by a lower aspect ratio, favored thin films predominantly on the channel base [32]. Both MMC1 and MMC3 benefited from these thin films, enhancing local evaporation rates [33]. Conversely, MMC2, with its symmetrical square geometry, produced relatively thicker liquid films, resulting in reduced convective heat transfer efficiency.

Fig. 6d presents the decomposition of total thermal resistance into conduction, convection, and advection components under identical heat

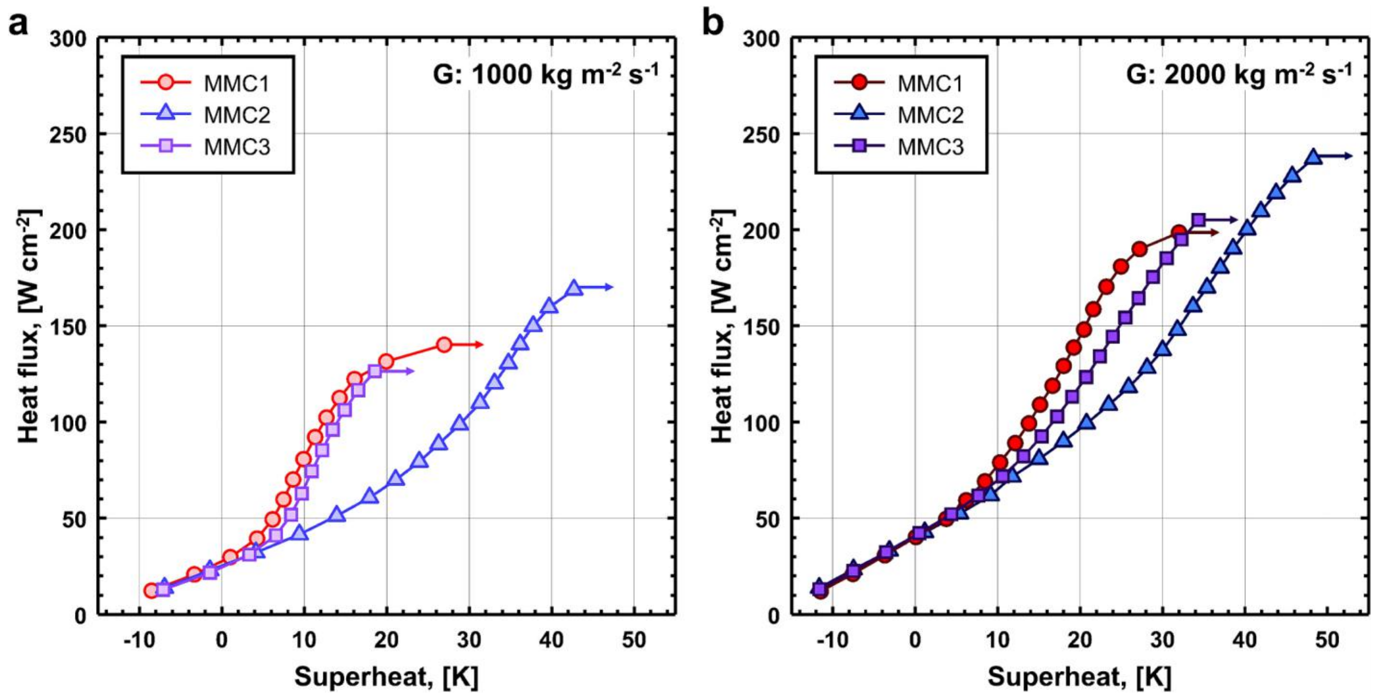

Fig. 4. Boiling curves of manifold microchannels under three geometric conditions. **a,** mass flux of 1000 kg m^{-2} s^{-1}, and **b,** 2000 kg m^{-2} s^{-1}.

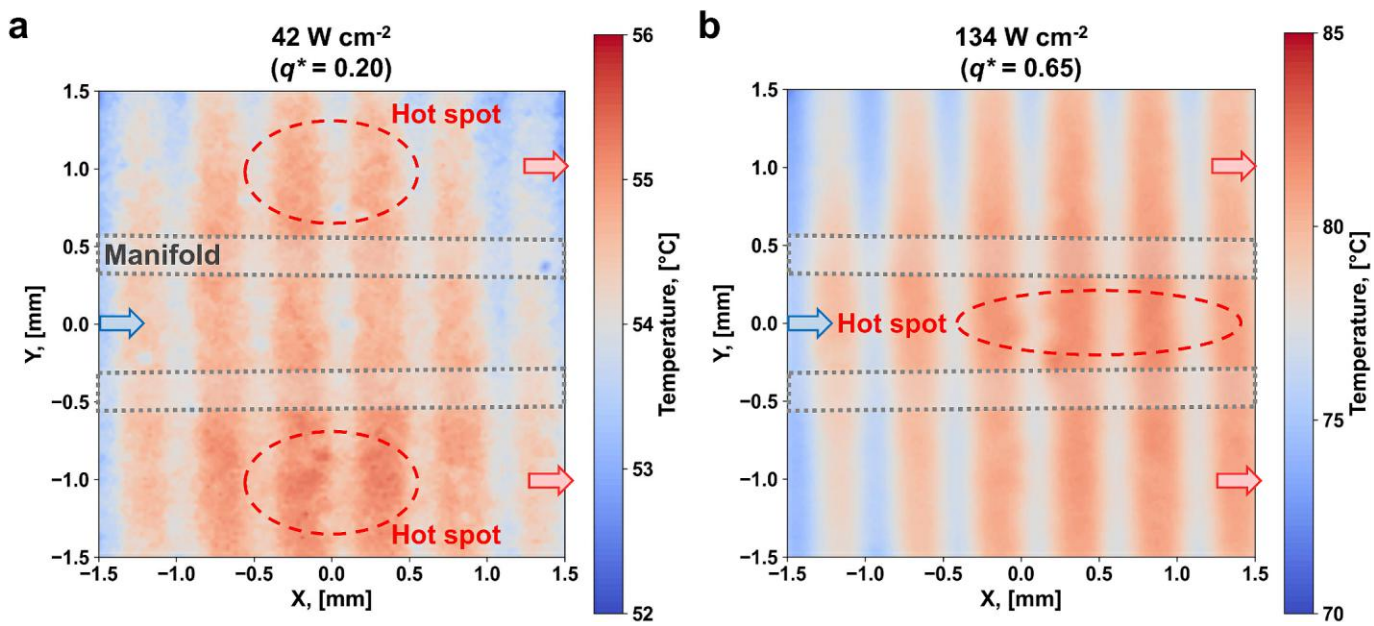

Fig. 5. Base temperature distribution within a 3 × 3 mm^2 zoomed-in region for MMC3 at 2000 kg m^{-2} s^{-1} under varying heat flux conditions: **a,** 42 W cm^{-2} ($q^* = 0.20$), and **b,** 134 W cm^{-2} ($q^* = 0.65$).

and mass flux conditions. Conduction resistance remained relatively constant across configurations due to the stable thermal conductivity of the silicon substrate. Advection resistance consistently declined with increased mass flow rates, reflecting enhanced sensible heat removal consistent with prior single-phase flow studies [13,34,35]. Convection resistance was highest for MMC2, directly attributed to its relatively thicker liquid films. In contrast, MMC1 and MMC3 displayed significantly lower convection resistances due to thinner liquid films formed along their narrow sidewalls and broader channel bases, facilitating more efficient heat transfer [36].

3.2. Thermal instability and flow visualization

With increasing vapor quality toward annular flow, intensified convective heat transfer coexisted with frequent local dry-out events, creating inherent instability [37,38]. Although porous CuIO surfaces initially promoted nucleate boiling, the thinning liquid film inevitably transitioned toward annular flow within microchannels at higher vapor qualities, leading to intermittent dry-out events. This instability evolved significantly depending on the microchannel aspect ratio, reflecting a geometric dependency similar to thermal resistance behavior. Consequently, an inherent trade-off emerged between achieving high CHF and

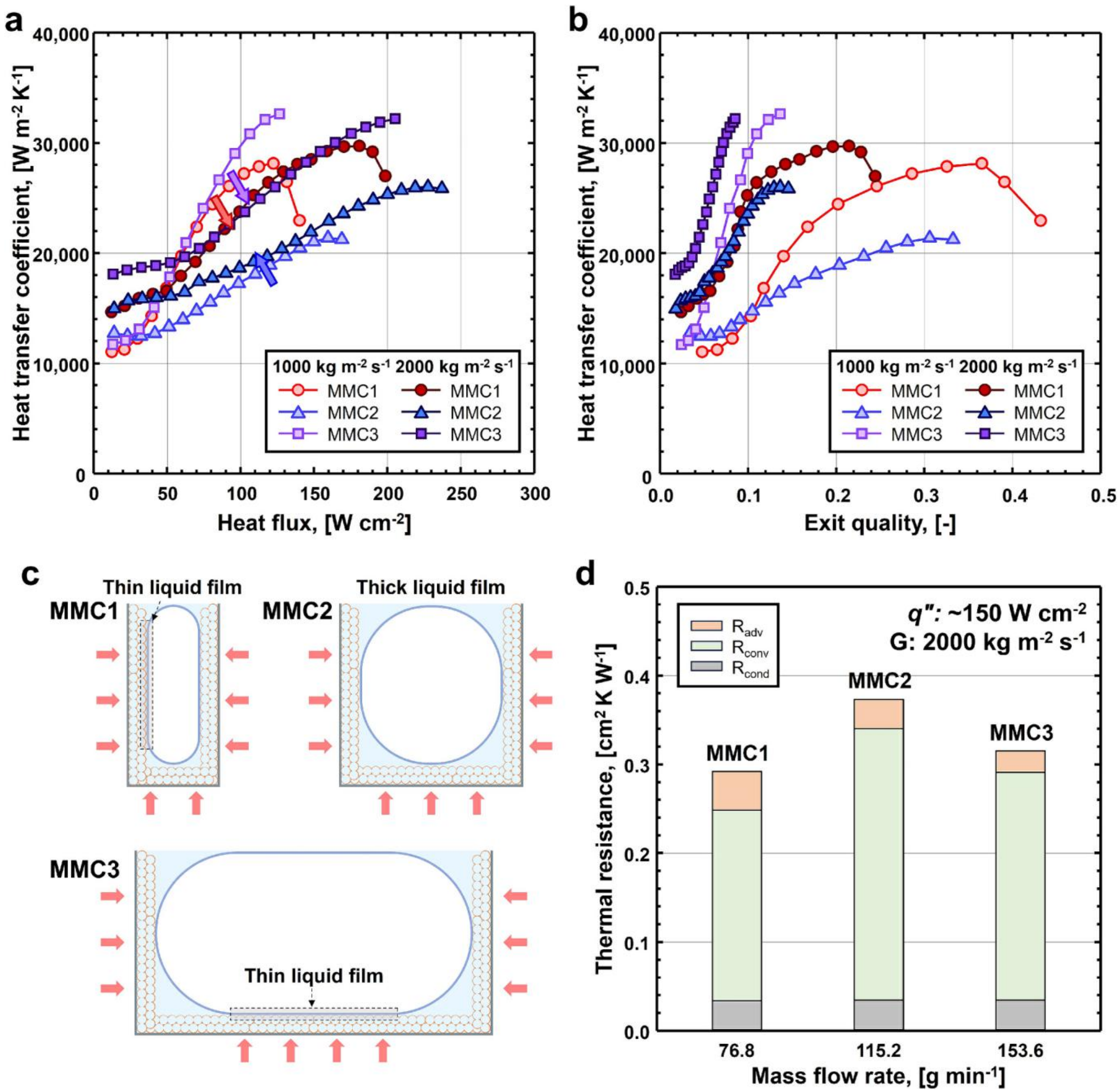

Fig. 6. The heat transfer coefficient, schematic representations of vapor dynamics within microchannels and thermal resistance. **a,** Heat transfer coefficient versus heat flux, **b,** Heat transfer coefficient versus exit thermodynamic vapor quality, **c,** Feasible flow behaviors based on different microchannel geometries, and **d,** Total thermal resistances–mass flow rate relationships and R_{adv}, R_{conv}, and R_{cond} at constant heat and mass flux (Table 3).

maintaining elevated heat transfer coefficients during flow boiling. This section explains the relationship between temperature instability and liquid film dynamics, linking these phenomena directly to flow behavior. In-situ visualization results distinctly identify the CHF triggering mechanisms within MMC devices.

Fig. 7(a1–a3) presents temporal fluctuations of base temperature recorded at $q^* = 1.0$ for MMC1, MMC2, and MMC3. The y-axis indicates instantaneous deviations from the mean base temperature, denoted as $T_b(t)$. At the lower mass flux of 1000 kg m^{-2} s^{-1}, temperature oscillations were markedly pronounced than those observed at the higher mass flux condition, with their magnitude influenced by geometrical conditions. MMC1 and MMC3 demonstrated a maximum temperature difference of about 7.3 °C and 8.0 °C, respectively, whereas MMC2 exhibited relatively mild fluctuations around 2.3 °C. The thermal stabilization trend at an increased mass flux of 2000 kg m^{-2} s^{-1} varied distinctly with geometry: MMC1 still displayed substantial (~2.8 °C), whereas MMC2 and MMC3 remained within the IR measurement uncertainty (±2 °C).

Based on these results, two primary instability mechanisms were identified, influenced by the interplay of mass flux and channel geometry. The first mechanism is thin-film breakup within microchannels [38]. At the lower mass flux of 1000 kg m^{-2} s^{-1}, MMC1 and MMC3 exhibited pronounced instability primarily due to rapid breakup of thin liquid films, enhancing evaporation but simultaneously causing significant temperature fluctuations. These films increased evaporation areas and promoted efficient heat transfer, but simultaneously facilitated film breakup easily and thereby intensified temperature instability [39]. Conversely, MMC2 displayed lower temperature variations, indicating that it maintained a relatively thicker liquid film, which was less susceptible to breakup. These observations align well with the previously discussed trends in heat transfer coefficients shown in Fig. 6c. The

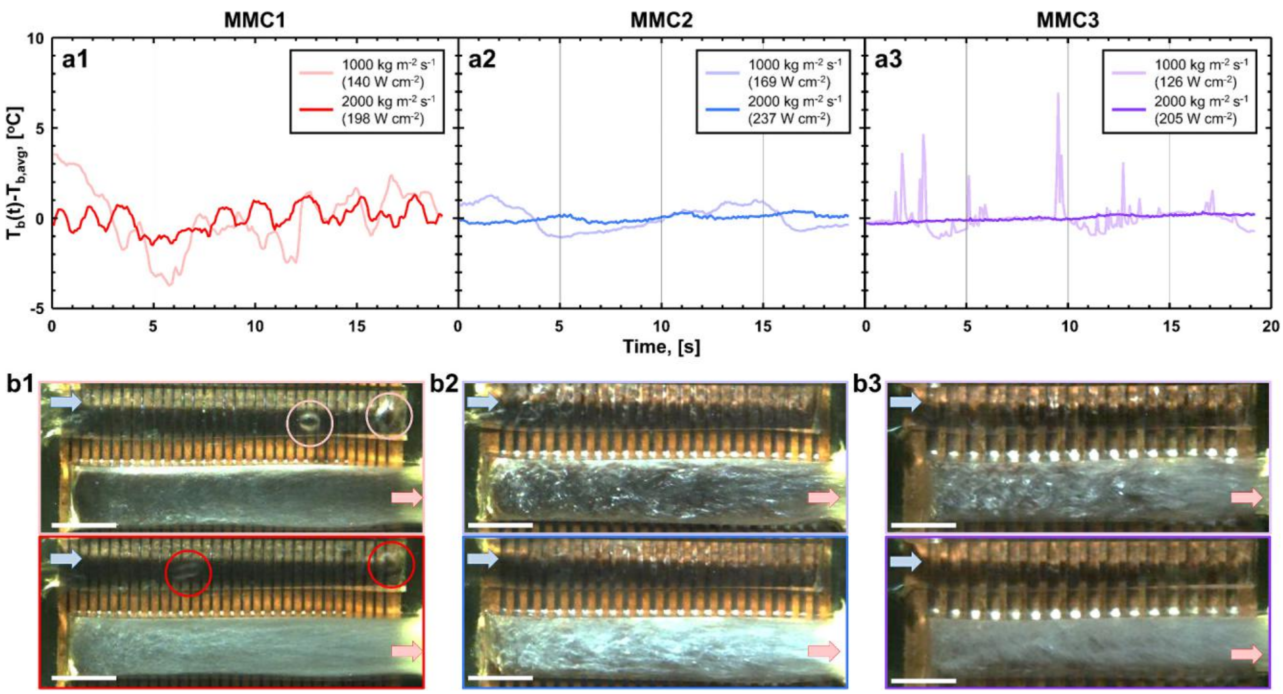

Fig. 7. Base temperature fluctuations at $q^* = 1.0$ and corresponding flow visualization. **a1**-**a3**, Time-dependent temperature variation by mass fluxes at the last data point, and **b1**-**b3**, High-speed visualization of unit cells for MMC1, MMC2, and MMC3 (top: 1000 kg m^{-2} s^{-1}, bottom: 2000 kg m^{-2} s^{-1}, and scale bars are 1 mm).

instability from film breakup was effectively mitigated as mass flux increased, which was primarily attributed to the sufficient liquid supply, suppressing the frequency of partial dry-out. Moreover, the microporous CuIO coatings further helped delay dry-out initiation by continuously replenishing the liquid at the higher mass flux condition, even at high heat flux ($q^* = 1.0$) [40–42]. In this regard, the favorable thermophysical properties of Novec-649, particularly its low surface tension, facilitated efficient liquid inflow into the porous CuIO structures via capillary action [43].

The second mechanism, liquid supply impediment due to inlet blockage, predominantly affected MMC1. In MMC1, narrow microchannel dimensions significantly amplified flow resistance, leading to persistent bubble accumulation within manifold inlet conduits (Fig. 7b1). These bubbles generated within the narrow microchannels occasionally migrated backward into the inlet conduits, driven by the high flow resistance associated with smaller channel dimensions. As a result, they impeded fresh liquid inflow continuously, thereby causing persistent temperature instability that remained unresolved even at higher mass flux conditions [44]. Conversely, MMC2 and MMC3, characterized by larger microchannel widths and thus lower flow resistances, exhibited minimal inlet blockage. Effective liquid supply in these geometries substantially improved thermal stability under increased mass flux conditions (Fig. 7b2 and b3).

Despite the distinct thermal stabilization behaviors observed in Fig. 7, backflow consistently propagated upstream through the manifold inlet plenum, promptly inducing CHF upon incremental heat flux increases (Fig. S4). Given the incremental heat flux step (~10 W cm^{-2}), the q^* value slightly exceeded unity (~1.06), surpassing CHF and thus necessitating immediate termination of experiments upon sudden temperature excursions to prevent device damage. Although backflow phenomena have previously been documented in microchannel boiling studies [45,46], comprehensive insights specifically addressing irreversible dry-out within MMC systems remain limited.

Fig. 8 elucidates the fundamental mechanism underlying backflow initiation and subsequent CHF in MMC devices, based on representative sequential visualization images immediately following the conditions depicted in Fig. 7b2 ($q^* > 1$). Specifically, inertial effects at the manifold inlet resulted in significant non-uniformity in coolant distribution

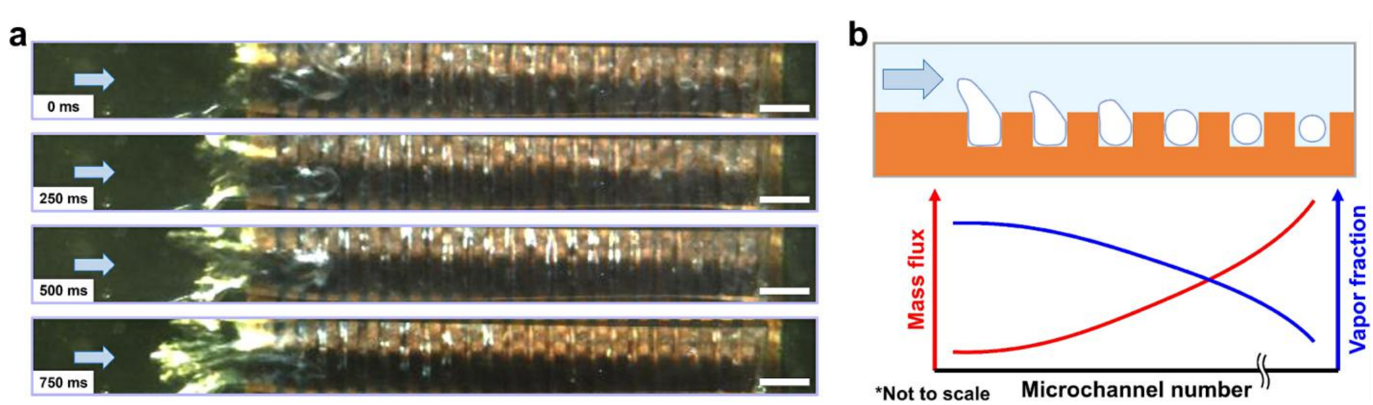

Fig. 8. Backflow visualization and depiction with approximate flow estimation. **a,** Backflow images from MMC2's manifold inlet plenum and conduit as a direct cause of CHF at 1000 kg m^{-2} s^{-1} ($q^* \approx 1.06$, and scale bars are 0.5 mm), and **b,** Schematic side view with anticipated liquid mass flux and vapor fraction (not to scale).

among microchannels, substantially reducing flow rates in channels proximal to the inlet plenum [47,48]. Conversely, channels located farther from the manifold inlet maintained higher coolant flow rates, thereby sustaining effective subcooling with minimal bubble accumulation [44]. Such pronounced flow maldistribution led to extensive bubble build-up and elevated local pressures in microchannels near the inlet [49]. Consequently, coolant inflow into these microchannels was severely impeded, progressively deteriorating local subcooling conditions and triggering backflow.

Once backflow occurred, it propagated upstream into the manifold inlet conduits, further exacerbating the flow imbalance and initiating an irreversible cascading effect that significantly compromised liquid replenishment [50]. This mechanism underscores why MMC2, characterized by its smaller effective evaporation area fraction, exhibited relatively lower convective heat transfer performance but more effectively suppressed dry-out initiation, thereby achieving a higher CHF compared to MMC1 and MMC3 [39,51].

3.3. Pressure drop

Fig. 9 presents the variation of pressure drop with increasing heat flux under different mass flux conditions. Overall, the pressure drop notably increased with rising heat flux, especially in the two-phase regime, due to vigorous bubble nucleation intensifying both frictional and accelerational pressure components. Even at relatively low heat flux conditions, average base temperatures generally exceeded the fluid saturation temperature (Fig. S5), signifying predominantly two-phase flow conditions across the entire tested heat flux range. Although previous research reported slight pressure drop reductions in single-phase flows caused by property variations [42], such trends were not observed in the current experiments.

Pressure drop consistently rose with increasing mass flux across all microchannel geometries [52]. MMC1 exhibited the highest pressure drop, reaching approximately 35.1 kPa at the maximum tested mass flux, primarily due to significant flow disturbances caused by frequent bubble clogging in its narrow manifold inlet conduits, greatly increasing flow resistance.

In contrast, MMC2 demonstrated the lowest maximum pressure drop (~26.6 kPa), despite achieving the highest CHF. This unique performance trade-off in MMC2 arose from its balanced geometry, which effectively delayed dry-out and suppressed bubble-induced instabilities by maintaining relatively thicker liquid films and stable coolant transport. However, these thicker films simultaneously reduced localized evaporation efficiency, resulting in comparatively lower heat transfer coefficients relative to MMC1 and MMC3, where thinner films significantly enhanced evaporation rates.

MMC3 exhibited intermediate pressure drop values, reflecting moderate flow resistance enabled by its wider channel structure and higher mass flow rates, balancing bubble dynamics with stable liquid replenishment. Previous studies on the relationship between microchannel aspect ratio and pressure drop remain inconclusive [53–55]; however, these results highlight that the specific geometric and flow conditions significantly influence both pressure drop and thermal performance in manifold microchannel systems. To complement these results, a benchmarking comparison is provided in the Supporting Information (Fig. S6, Supplementary Notes S4), which contextualizes the present results against related studies [56–60].

4. Conclusions

This study systematically investigated the thermal–hydraulic behavior of CuIO-coated manifold microchannel heat sinks with Novec-649 as the working fluid. The results demonstrate how channel geometry and mass flux dictate the balance between CHF, heat transfer efficiency, and flow stability.

Square channels (MMC2) achieved the highest CHF of 237 W cm^{-2} while maintaining a relatively low pressure drop of 26.6 kPa, enabled by stable flow distribution and thicker liquid films. Their performance, however, was limited by a lower heat transfer coefficient of ~26,000 W m^{-2} K^{-1}. High-aspect-ratio channels (MMC1) initially delivered superior heat transfer through thin-film evaporation, but efficiency declined at higher heat flux due to restricted liquid replenishment and localized dry-out. Low-aspect-ratio channels (MMC3) sustained stable evaporation and reached heat transfer coefficients up to 33,000 W m^{-2} K^{-1}, though with lower CHF compared to MMC2.

The observed trade-off between CHF and heat transfer coefficient originates from liquid film dynamics imposed by channel geometry. Instability patterns further reflected this dependence: MMC1 showed

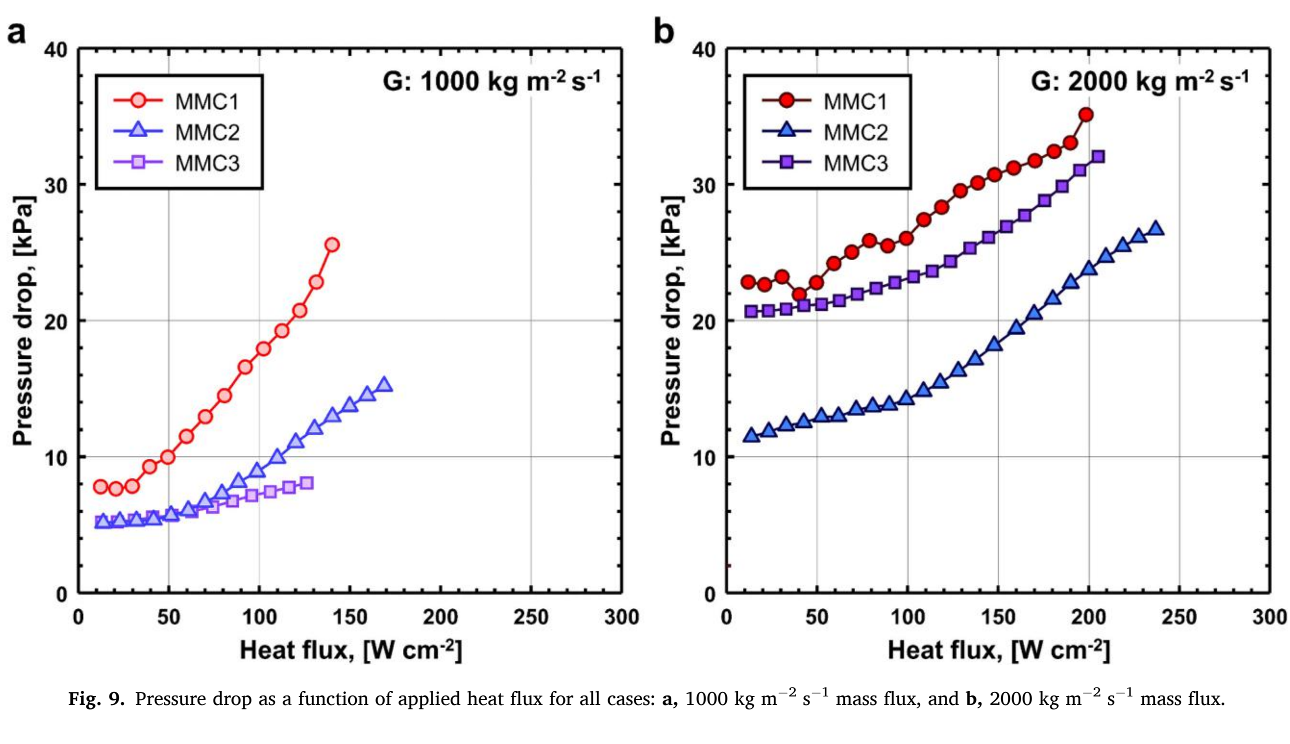

Fig. 9. Pressure drop as a function of applied heat flux for all cases: **a,** 1000 kg m^{-2} s^{-1} mass flux, and **b,** 2000 kg m^{-2} s^{-1} mass flux.

persistent oscillations from inlet bubble blockage, MMC3 exhibited early fluctuations from thin-film breakup that diminished at higher mass flux, and MMC2 consistently maintained minimal instability. CHF was triggered by backflow from inlet-side microchannels, caused by uneven liquid distribution in the manifold, which reduced local mass flux and weakened subcooling. Pressure drops followed the same geometric trend, with MMC1 presenting the highest resistance, MMC2 the lowest, and MMC3 an intermediate level. These experimentally validated results provide mechanistic insight into how geometry governs boiling performance, offering quantitative benchmarks and design guidance for two-phase cooling in high-power electronic devices and data-intensive applications.

CRediT authorship contribution statement

Youngseob Lee: Writing – original draft, Methodology, Investigation, Formal analysis, Data curation. **Daeyoung Kong:** Writing – original draft, Methodology, Investigation, Formal analysis, Conceptualization. **Jaewon Hwang:** Visualization, Validation, Investigation. **Seokwon Jeong:** Writing – review & editing, Formal analysis, Data curation. **Jungwan Cho:** Writing – review & editing, Supervision, Project administration, Funding acquisition. **Hyoungsoon Lee:** Writing – review & editing, Supervision, Project administration, Funding acquisition.

Declaration of competing interest

The authors declare that they have no known competing financial interests or personal relationships that could have appeared to influence the work reported in this paper.

Acknowledgments

This work was supported by the National Research Foundation of Korea (NRF) grant funded by the Korea government (MSIT) (Nos. RS-2024-00411577 and RS-2024-00353227), and the Chung-Ang University Graduate Research Scholarship in 2024.

Appendix A. Supplementary data

Supplementary data to this article can be found online at https://doi.org/10.1016/j.applthermaleng.2025.128353.

Data availability

Data will be made available on request.

References

[1] I.L. Markov, Limits on fundamental limits to computation, Nature 512 (2014) 147–154, https://doi.org/10.1038/nature13570.
[2] J. Shalf, The future of computing beyond Moore's Law, Phil. Trans. R. Soc. A 378 (2020) 20190061, https://doi.org/10.1098/rsta.2019.0061.
[3] Y. Sun, N.B. Agostini, S. Dong, D. Kaeli, Summarizing CPU and GPU Design Trends with Product Data, 2020. http://arxiv.org/abs/1911.11313 (Accessed March 28, 2024).
[4] J.-H. Han, X. Guo, K. Skadron, M.R. Stan, From 2.5D to 3D chiplet systems: investigation of thermal implications with HotSpot 7.0, in: 2022 21st IEEE Intersociety Conference on Thermal and Thermomechanical Phenomena in Electronic Systems (iTherm), IEEE, San Diego, CA, USA, 2022, pp. 1–6, https://doi.org/10.1109/iTherm54085.2022.9899649.
[5] Y. Chen, V. Sankatali, S. Mishra, J. Ryckaert, J. Myers, D. Biswas, Thermal implications in scaling high-performance server 3D chiplet-based 2.5D SoC from FinFET to nanosheet, in: IEEE Computer Society Annual Symposium on VLSI (ISVLSI), IEEE, Knoxville, TN, USA, 2024, pp. 45–50, https://doi.org/10.1109/ISVLSI61997.2024.00020.
[6] P. Wang, P. McCluskey, A. Bar-Cohen, Two-phase liquid cooling for thermal management of IGBT power electronic module, J. Electron. Packag. 135 (2013) 021001, https://doi.org/10.1115/1.4023215.
[7] Z. He, Y. Yan, Z. Zhang, Thermal management and temperature uniformity enhancement of electronic devices by micro heat sinks: a review, Energy 216 (2021) 119223, https://doi.org/10.1016/j.energy.2020.119223.
[8] N. Zhang, B. Jiao, Y. Ye, Y. Kong, X. Du, R. Liu, B. Cong, L. Yu, S. Jia, K. Jia, Embedded cooling method with configurability and replaceability for multi-chip electronic devices, Energ. Conver. Manage. 253 (2022) 115124, https://doi.org/10.1016/j.enconman.2021.115124.
[9] X. Ji, X. Ma, X. Yang, J. Wei, B. Sundén, Jet array impingement boiling in compact space for high heat flux cooling, Appl. Therm. Eng. 219 (2023) 119538, https://doi.org/10.1016/j.applthermaleng.2022.119538.
[10] J.D. Benther, J.D. Pelaez-Restrepo, C. Stanley, G. Rosengarten, Heat transfer during multiple droplet impingement and spray cooling: review and prospects for enhanced surfaces, Int. J. Heat Mass Transf. 178 (2021) 121587, https://doi.org/10.1016/j.ijheatmasstransfer.2021.121587.
[11] S.-M. Kim, I. Mudawar, Review of databases and predictive methods for heat transfer in condensing and boiling mini/micro-channel flows, Int. J. Heat Mass Transf. 77 (2014) 627–652, https://doi.org/10.1016/j.ijheatmasstransfer.2014.05.036.
[12] D. Copeland, M. Behnia, W. Nakayama, Manifold microchannel heat sinks: isothermal analysis, in: InterSociety Conference on Thermal Phenomena in Electronic Systems, I-THERM V, 1996: pp. 251–257. doi: 10.1109/ITHERM.1996.534570.
[13] R. Van Erp, R. Soleimanzadeh, L. Nela, G. Kampitsis, E. Matioli, Co-designing electronics with microfluidics for more sustainable cooling, Nature 585 (2020) 211–216, https://doi.org/10.1038/s41586-020-2666-1.
[14] X. Huang, W. Tang, Z. Wu, Y. Wang, L. Luo, K. Sheng, Flow boiling of HFE-7100 for cooling multi-chip modules using manifold microchannels, Appl. Therm. Eng. 259 (2025) 124929, https://doi.org/10.1016/j.applthermaleng.2024.124929.
[15] K.P. Drummond, D. Back, M.D. Sinanis, D.B. Janes, D. Peroulis, J.A. Weibel, S. V. Garimella, A hierarchical manifold microchannel heat sink array for high-heat-flux two-phase cooling of electronics, Int. J. Heat Mass Transf. 117 (2018) 319–330, https://doi.org/10.1016/j.ijheatmasstransfer.2017.10.015.
[16] K. Tang, Y. Huang, G. Lin, Y. Guo, J. Huang, H. Lin, H. Zhang, Q. Yang, J. Miao, Thermal-hydraulic performance of ammonia in manifold microchannel heat sink, Appl. Therm. Eng. 232 (2023) 121000, https://doi.org/10.1016/j.applthermaleng.2023.121000.
[17] K.P. Drummond, J.A. Weibel, S.V. Garimella, Two-phase flow morphology and local wall temperatures in high-aspect-ratio manifold microchannels, Int. J. Heat Mass Transf. 153 (2020) 119551, https://doi.org/10.1016/j.ijheatmasstransfer.2020.119551.
[18] J. Zhou, F. Zhou, Q. Zhao, M. Lu, Q. Li, X. Chen, Flow boiling heat transfer in manifold microchannels with topologically optimized configurations, Int. Commun. Heat Mass Transfer 161 (2025) 108555, https://doi.org/10.1016/j.icheatmasstransfer.2024.108555.
[19] K. Kim, D. Kong, Y. Kim, B. Jang, J. Cho, H.-J. Kwon, H. Lee, Enhanced boiling heat transfer via microporous copper surface integration in a manifold microgap, Appl. Therm. Eng. 241 (2024) 122325, https://doi.org/10.1016/j.applthermaleng.2023.122325.
[20] E.M. Abo-Zahhad, S. Ookawara, A. Radwan, S. Memon, Y. Yang, M.F. El-Kady, A. H. El-Shazly, Flow boiling in a four-compartment heat sink for high-heat flux cooling: a parametric study, Energ. Conver. Manage. 230 (2021) 113778, https://doi.org/10.1016/j.enconman.2020.113778.
[21] D. Kong, H. Kwon, B. Jang, H.-J. Kwon, M. Asheghi, K.E. Goodson, H. Lee, Extreme heat flux cooling from functional copper inverse opal-coated manifold microchannels, Energ. Conver. Manage. 315 (2024) 118809, https://doi.org/10.1016/j.enconman.2024.118809.
[22] C. Zhang, J.W. Palko, M.T. Barako, M. Asheghi, J.G. Santiago, K.E. Goodson, Enhanced capillary-fed boiling in copper inverse opals via template sintering, Adv. Funct. Mater. 28 (2018), https://doi.org/10.1002/adfm.201803689.
[23] K.K. Wong, K.C. Leong, Nucleate flow boiling enhancement on engineered three-dimensional porous metallic structures in FC-72, Appl. Therm. Eng. 159 (2019) 113846, https://doi.org/10.1016/j.applthermaleng.2019.113846.
[24] Y. Lee, K. Kim, Y. Kim, D. Kong, J. Park, D. Son, S. Kang, S. Hong, H. Lee, Micro-/Nanohierarchical Surfaces for Enhanced Pool Boiling in Large-Area Silicon Multichips, Small Struct. n/a (n.d.) 2400512. doi: 10.1002/sstr.202400512.
[25] Y.-F. Wang, J.-T. Wu, Thermal performance predictions for an HFE-7000 direct flow boiling cooled battery thermal management system for electric vehicles, Energ. Conver. Manage. 207 (2020) 112569, https://doi.org/10.1016/j.enconman.2020.112569.
[26] W. Qu, I. Mudawar, Flow boiling heat transfer in two-phase micro-channel heat sinks—I. Experimental investigation and assessment of correlation methods, Int. J. Heat Mass Transf. 46 (2003) 2755–2771, https://doi.org/10.1016/S0017-9310(03)00041-3.
[27] S.-M. Kim, I. Mudawar, Universal approach to predicting saturated flow boiling heat transfer in mini/micro-channels – Part II. Two-phase heat transfer coefficient, Int. J. Heat Mass Transfer 64 (2013) 1239–1256, https://doi.org/10.1016/j.ijheatmasstransfer.2013.04.014.
[28] J. Mathew, P.-S. Lee, T. Wu, C.R. Yap, Experimental study of flow boiling in a hybrid microchannel-microgap heat sink, Int. J. Heat Mass Transf. 135 (2019) 1167–1191, https://doi.org/10.1016/j.ijheatmasstransfer.2019.02.033.
[29] F. Municchi, C.N. Markides, O.K. Matar, M. Magnini, Computational study of bubble, thin-film dynamics and heat transfer during flow boiling in non-circular microchannels, Appl. Therm. Eng. 238 (2024) 122039, https://doi.org/10.1016/j.applthermaleng.2023.122039.
[30] T.-H. Yen, M. Shoji, F. Takemura, Y. Suzuki, N. Kasagi, Visualization of convective boiling heat transfer in single microchannels with different shaped cross-sections,

Int. J. Heat Mass Transf. 49 (2006) 3884–3894, https://doi.org/10.1016/j.ijheatmasstransfer.2005.12.024.
[31] T. Harirchian, S.V. Garimella, A comprehensive flow regime map for microchannel flow boiling with quantitative transition criteria, Int. J. Heat Mass Transf. 53 (2010) 2694–2702, https://doi.org/10.1016/j.ijheatmasstransfer.2010.02.039.
[32] A.H. Al-Zaidi, M.M. Mahmoud, T.G. Karayiannis, Effect of aspect ratio on flow boiling characteristics in microchannels, Int. J. Heat Mass Transf. 164 (2021) 120587, https://doi.org/10.1016/j.ijheatmasstransfer.2020.120587.
[33] J.R. Thome, V. Dupont, A.M. Jacobi, Heat transfer model for evaporation in microchannels. Part I: Presentation of the model, Int. J. Heat Mass Transfer 47 (2004) 3375–3385, https://doi.org/10.1016/j.ijheatmasstransfer.2004.01.006.
[34] K.W. Jung, C.R. Kharangate, H. Lee, J. Palko, F. Zhou, M. Asheghi, E.M. Dede, K. E. Goodson, Embedded cooling with 3D manifold for vehicle power electronics application: single-phase thermal-fluid performance, Int. J. Heat Mass Transf. 130 (2019) 1108–1119, https://doi.org/10.1016/j.ijheatmasstransfer.2018.10.108.
[35] Y.J. Lee, S.J. Kim, Experimental investigation on thermal-hydraulic performance of manifold microchannel with pin-fins for ultra-high heat flux cooling, Int. J. Heat Mass Transf. 224 (2024) 125336, https://doi.org/10.1016/j.ijheatmasstransfer.2024.125336.
[36] M. Magnini, O.K. Matar, Numerical study of the impact of the channel shape on microchannel boiling heat transfer, Int. J. Heat Mass Transf. 150 (2020) 119322, https://doi.org/10.1016/j.ijheatmasstransfer.2020.119322.
[37] A.M. Jacobi, J.R. Thome, Heat transfer model for evaporation of elongated bubble flows in microchannels, J. Heat Transfer 124 (2002) 1131–1136, https://doi.org/10.1115/1.1517274.
[38] T. Chen, S.V. Garimella, Local heat transfer distribution and effect of instabilities during flow boiling in a silicon microchannel heat sink, Int. J. Heat Mass Transf. (2011) 3179–3190, https://doi.org/10.1016/j.ijheatmasstransfer.2011.04.012.
[39] S. Bigham, A. Fazeli, S. Moghaddam, Physics of microstructures enhancement of thin film evaporation heat transfer in microchannels flow boiling, Sci. Rep. 7 (2017) 44745, https://doi.org/10.1038/srep44745.
[40] D. Deng, W. Wan, H. Shao, Y. Tang, J. Feng, J. Zeng, Effects of operation parameters on flow boiling characteristics of heat sink cooling systems with reentrant porous microchannels, Energ. Conver. Manage. 96 (2015) 340–351, https://doi.org/10.1016/j.enconman.2015.02.072.
[41] W. Li, S. Yang, Y. Chen, C. Li, Z. Wang, Tesla valves and capillary structures-activated thermal regulator, Nat. Commun. 14 (2023) 3996, https://doi.org/10.1038/s41467-023-39289-5.
[42] S. Wang, H.-H. Chen, C.-L. Chen, Enhanced flow boiling in silicon nanowire-coated manifold microchannels, Appl. Therm. Eng. 148 (2019) 1043–1057, https://doi.org/10.1016/j.applthermaleng.2018.11.125.
[43] N.V. Upot, A. Bakhshi, K. Fazle Rabbi, F. Lu, A.M. Jacobi, N. Miljkovic, Enhanced refrigerant flow boiling heat transfer in microstructured finned surfaces, Int. J. Heat Mass Transf. 207 (2023) 123999, https://doi.org/10.1016/j.ijheatmasstransfer.2023.123999.
[44] Y. Luo, J. Zhang, W. Li, A comparative numerical study on two-phase boiling fluid flow and heat transfer in the microchannel heat sink with different manifold arrangements, Int. J. Heat Mass Transf. 156 (2020) 119864, https://doi.org/10.1016/j.ijheatmasstransfer.2020.119864.
[45] W. Qu, I. Mudawar, Measurement and correlation of critical heat flux in two-phase micro-channel heat sinks, Int. J. Heat Mass Transf. 47 (2004) 2045–2059, https://doi.org/10.1016/j.ijheatmasstransfer.2003.12.006.
[46] Y.K. Prajapati, P. Bhandari, Flow boiling instabilities in microchannels and their promising solutions – a review, Exp. Therm Fluid Sci. 88 (2017) 576–593, https://doi.org/10.1016/j.expthermflusci.2017.07.014.
[47] L. Boteler, N. Jankowski, P. McCluskey, B. Morgan, Numerical investigation and sensitivity analysis of manifold microchannel coolers, Int. J. Heat Mass Transf. 55 (2012) 7698–7708, https://doi.org/10.1016/j.ijheatmasstransfer.2012.07.073.
[48] D. Kong, Y. Kim, M. Kang, E. Song, Y. Hong, H.S. Kim, K.J. Rah, H.G. Choi, D. Agonafer, H. Lee, A holistic approach to thermal-hydraulic design of 3D manifold microchannel heat sinks for energy-efficient cooling, Case Stud. Therm. Eng. 28 (2021) 101583, https://doi.org/10.1016/j.csite.2021.101583.
[49] H.-G. Kim, S. Senguttuvan, H.-C. Shin, S.-M. Kim, Experimental investigation of flow boiling instability and associated pressure fluctuations in a mini-channel heat sink, Appl. Therm. Eng. 258 (2025) 124681, https://doi.org/10.1016/j.applthermaleng.2024.124681.
[50] Y.K. Prajapati, M. Pathak, Mohd. Kaleem Khan, A comparative study of flow boiling heat transfer in three different configurations of microchannels, Int. J. Heat Mass Transf. 85 (2015) 711–722, https://doi.org/10.1016/j.ijheatmasstransfer.2015.02.016.
[51] M.J. Inanlu, V. Ganesan, N.V. Upot, C. Wang, Z. Suo, K. Fazle Rabbi, P. Kabirzadeh, A. Bakhshi, W. Fu, T.S. Thukral, V. Belosludtsev, J. Li, N. Miljkovic, Unveiling the fundamentals of flow boiling heat transfer enhancement on structured surfaces, Sci. Adv. 10 (2024) eadp8632, https://doi.org/10.1126/sciadv.adp8632.
[52] S. Yang, J. Li, B. Cao, Z. Wu, K. Sheng, Investigation of Z-type manifold microchannel cooling for ultra-high heat flux dissipation in power electronic devices, Int. J. Heat Mass Transf. 218 (2024) 124792, https://doi.org/10.1016/j.ijheatmasstransfer.2023.124792.
[53] B. Markal, O. Aydin, M. Avci, Effect of aspect ratio on saturated flow boiling in microchannels, Int. J. Heat Mass Transf. 93 (2016) 130–143, https://doi.org/10.1016/j.ijheatmasstransfer.2015.10.024.
[54] S.G. Singh, A. Kulkarni, S.P. Duttagupta, B.P. Puranik, A. Agrawal, Impact of aspect ratio on flow boiling of water in rectangular microchannels, Exp. Therm Fluid Sci. 33 (2008) 153–160, https://doi.org/10.1016/j.expthermflusci.2008.07.014.
[55] W.-T. Yan, W.-B. Ye, C. Li, Effect of aspect ratio on saturated boiling flow in microchannels with nonuniform heat flux, Heat Transfer—Asian Res. 48 (2019) 3312–3327, https://doi.org/10.1002/htj.21543.
[56] L.-H. Chien, Y.-T. Cheng, Y.-L. Lai, W.-M. Yan, M. Ghalambaz, Experimental and numerical study on convective boiling in a staggered array of micro pin-fin microgap, Int. J. Heat Mass Transf. 149 (2020) 119203, https://doi.org/10.1016/j.ijheatmasstransfer.2019.119203.
[57] W. Chang, K. Luo, W. Li, C. Li, Enhanced flow boiling of HFE-7100 in silicon microchannels with nanowires coated micro-pinfins, Appl. Therm. Eng. 216 (2022) 119064, https://doi.org/10.1016/j.applthermaleng.2022.119064.
[58] H. Shang, G. Xia, R. Li, S. Miao, Experimental study on flow boiling heat transfer of HFE-7100 in minichannel heat sinks for professional-grade server chips cooling, Int. Commun. Heat Mass Transfer 164 (2025) 108825, https://doi.org/10.1016/j.icheatmasstransfer.2025.108825.
[59] Z. Zhang, L. Jia, C. Dang, Y. Ding, Experimental study on flow boiling characteristics of R134a inside high-heat-flux microchannels, Int. J. Heat Fluid Flow 107 (2024) 109372, https://doi.org/10.1016/j.ijheatfluidflow.2024.109372.
[60] F. Yang, W. Li, X. Dai, C. Li, Flow boiling heat transfer of HFE-7000 in nanowire-coated microchannels, Appl. Therm. Eng. 93 (2016) 260–268, https://doi.org/10.1016/j.applthermaleng.2015.09.097.